THE PENNSYLVANIA STATE UNIVERSITY
SCHREYER HONORS COLLEGE

DEPARTMENT OF PHYSICS

RESTORATION OF A LOW TEMPERATURE SCANNING TUNNELING MICROSCOPE

Baird Bankovic
SPRING 2024

A thesis
submitted in partial fulfillment
of the requirements
for baccalaureate degrees
in Physics
with honors in Physics

Reviewed and approved* by the following:

Nitin Samarth
Professor of Physics
Thesis Supervisor
Honors Adviser

Eric Hudson
Associate Professor of Physics
Research Advisor

Anthony Richardella
Assistant Research Professor
Faculty Reader

*Signatures are on file in the Schreyer Honors College.

Abstract

Scanning tunneling microscopy is a technique that enables the study of the surfaces of materials with sub-nanometer resolution. A scanning tunneling microscope (STM) gives local electronic information about the surface and is an invaluable analysis technique in modern condensed matter physics. The goal of my project was to restore an existing low temperature STM which had fallen into disrepair. This thesis outlines the restoration process, along with a description of the supporting techniques that were necessary. In parallel with the restoration process, I also developed an automated tungsten tip fabricator for making atomically sharp tips for the STM. This is an original design that I have shared on an open source website. Additionally, I explored the use of a low temperature transimpedance preamplifier that would improve the performance of our STM and tested a number of operational amplifiers that could be used to this end.

Table of Contents

List of Figures

List of Tables

Acknowledgements

I would like to thank a number of individuals where were *instrumental* to my development as an engineer and a growing scientist at Penn State. First, to my advisor Professor Nitin Samarth who gave me the opportunity to work on a number of systems, only one of which has made it into this thesis. Additionally, he has supported me throughout the past three years in his lab, which I am very grateful for. I also want to thank Professor Eric Hudson who gave me the opportunity to restore SNIPE, this was an incredible learning experience for me!

Next, to Research Professor Anthony Richardella, whom has spent many late nights with me in the lab, teaching me the nuanced details of working in an experimental physics lab. Anthony was always the first person I went to if I had questions about physics, electronics, or UHV practices. Many of the things I did in my time as an undergraduate would not have been possible if it were not for Anthony's expertise, thanks for all the fish.

To my fellow lab mates in the Samarth group whom made my time here more productive and enjoyable, Emma Steinebronn, Jyotirmay Dwivedi, and especially Max Stanley whom has helped me better understand solid state physics. Also to Luc Schrauf, who put up with the many late nights venting, lifting, cleaning, and troubleshooting electronics on SNIPE, along with my dry sense of humor for the past eight months.

Most of all, I extend my thanks to my parents, Amy and Dan Bankovic, whom have always supported my interest in the physical sciences, even if that means sending a model rocket into the window of our house. I could not ask for more supportive parents.

Chapter 1

Overview of SNIPE

1.1 Introduction

In 1950, Erwin Müller and his student Kanwar Bahadur developed an atomic resolution field emission electron microscope at Penn State, becoming the first people to observe isolated atoms [3]. The drive to observe the physical world at smaller and smaller length scales led to the first controllable vacuum gap tunneling measurements in 1981 at IBM's Zurich research lab [4]. This work laid the foundation to build a scanning tunneling microscope (STM), which are capable of resolving individual atoms in real space on the surface of a material, and can even be used for manipulating individual atoms [5].

An STM creates images of atoms on the surface of materials by measuring the current of electrons due to quantum tunneling between the point of a sharp metal tip and the surface of the sample. Quantum tunneling of electrons in this context describes a process whereby electrons "jump" from the tip to the sample via a process that would be classically forbidden. Quantum mechanics allows such a process because of the wave nature of the electrons. A more detailed description is given in section 1.1.1.

In an STM, quantum tunneling of electrons is used as a proxy to measure the tip-sample distance. By applying a small potential difference between the tip and sample ($\sim$2V), and bringing the tip within $\sim$2 angstroms of the sample's surface, an electrical tunneling current of $\sim$1 nanoamp can be measured. The tunneling current changes exponentially with the tip-sample separation, thus allowing one to measure small changes in distance. To create an image, the tip scans line by line across the sample. As the tip rasters across the sample, changes in the atomic wave functions (which can be schematically viewed as the spherical shape of atoms) causes local high and low points on the topography, which is detected in the tunneling current. Fig. 1.1 shows an illustration of a sharp tip scanning along the surface of the sample.

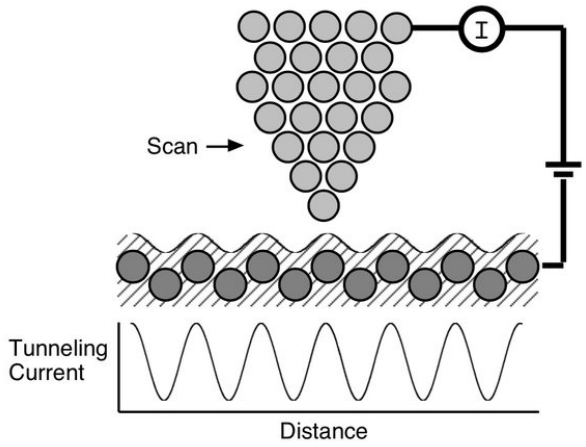

Figure 1.1: STM topography scanning principle [1]

1.1.1 STM Theoretical Model

In this section, I derive an expression for the tunneling current by modeling the STM tip-sample system as being separated by a 1-D square potential barrier. Consider a quantum particle approaching a potential barrier as seen in Fig. 1.2. If $E >> V_0$, the particle will cross the barrier as a plane wave whose propagation is modified by the presence of the barrier. If $E < V_0$, the particle must tunnel through the barrier. We can solve the time-independent Schrödinger equation, $\frac{-\hbar^2}{2m}\frac{\partial^2}{\partial x^2}\psi(x) + V(x)\psi(x) = E\psi(x)$, by using the usual boundary conditions (continuity of the wave function and its derivative) in regions I, II, and III (see Fig. 1.2).

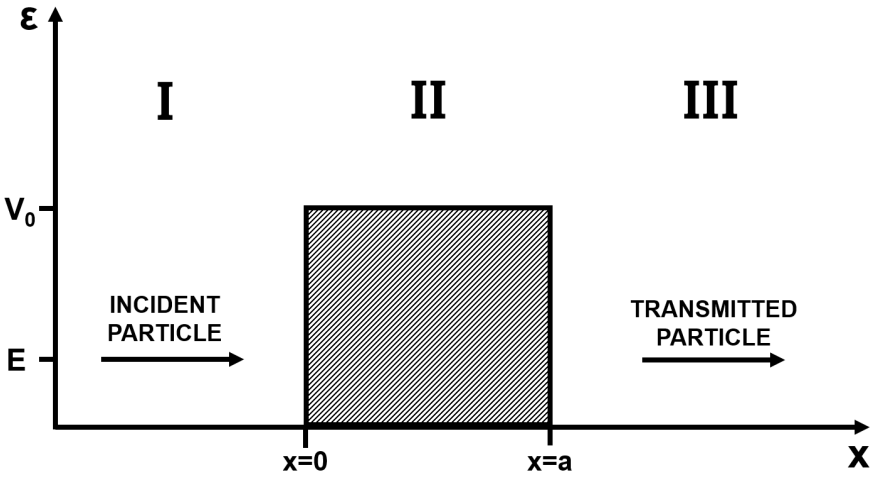

Figure 1.2: Diagram of 1D tunneling barrier.

Region I and III: The time-independent Schrödinger equation is given by: $\frac{-\hbar^2}{2m}\frac{\partial^2}{\partial x^2}\psi(x) = E\psi(x)$ since $V(x) = 0$. Moving $\frac{-\hbar^2}{2m}$ to the other side,

$$\frac{\partial^2}{\partial x^2}\psi(x) = -\frac{2m}{\hbar^2}E\psi(x). \tag{1.1}$$

Let $\kappa_0^2 = \frac{2mE}{\hbar}$,

$$\frac{\partial^2}{\partial x^2}\psi(x) + \kappa_0^2 E\psi(x) = 0 \tag{1.2}$$

In regions I and III, this differential equation with the appropriate boundary conditions has solutions

$$\psi_I(x) = Ae^{i\kappa_0 x} + Be^{-i\kappa_0 x}, \text{ and } \psi_{III}(x) = Ce^{i\kappa_0 x} + De^{-i\kappa_0 x} \tag{1.3}$$

where A, B, C and D are normalization factors. Since the incident particle is traveling to the right in region III, $D = 0$.

Region II: In this region, $V(x) = V_0$, and if $E < V_0$, this is the classically forbidden region. The time-independent Schrödinger becomes

$$-\frac{\hbar^2}{2m}\frac{\partial^2}{\partial x^2}\psi(x) + (V_0 - E)\psi(x) = 0. \tag{1.4}$$

Let $\kappa_{II}^2 = \frac{2m(V_0-E)}{\hbar}$, and we get

$$-\frac{\partial^2}{\partial x^2}\psi(x) + \kappa_{II}^2\psi(x) = 0. \tag{1.5}$$

This has solutions which are real due to normalizability,

$$\psi_{II}(x) = Fe^{\kappa_{II}x} + Ge^{-\kappa_{II}x}. \tag{1.6}$$

Applying continuity boundary conditions to the wave function solutions, we get a system of equa-

tions that can be used to solve for the coefficients.

$$A + B = F + G \tag{1.7}$$

$$i\kappa_0 A - i\kappa_0 B = \kappa_{II} F - \kappa_{II} G \tag{1.8}$$

$$Fe^{\kappa_{II} a} + Ge^{-\kappa_{II} a} = Ce^{i\kappa_{II} a} \tag{1.9}$$

$$Fe^{\kappa_{II} a} - G\kappa_{II} e^{-\kappa_{II} a} = i\kappa_0 Ce^{i\kappa_0 a} \tag{1.10}$$

Additionally, we define transmission and reflection coefficients that provide the probability of the incident particle being transmitted or reflected across the barrier. The final constraint needed is the sum of the transmission and reflection coefficients is equal to 1.

$$T = \frac{C^* C}{A^* A} \text{ , and } R = \frac{B * B}{A^* A} \text{ with constraint } T + R = 1 \tag{1.11}$$

The coefficients A, B, C, F, and G can be determined by using the system of five equations 1.7 - 1.11. For any physical measurement, the important quantities are the transmission and reflection coefficients. There solutions are given in equations 1.12 and 1.13.

$$T = \left(\frac{V_0^2}{4E(V_0 - E)} sinh^2(\kappa_{II} a) + 1 \right)^{-1} \tag{1.12}$$

$$R = 1 - T \tag{1.13}$$

If the transmission coefficient is much less than 1, it can be approximated as a decaying exponential with barrier width. This is often done for modeling of the tunnel junction formed by the tip and sample in STM, hence why a logarithmic amplifier is typically used for the linear feedback loop [6]. Fig. 1.3 shows a plot of the transmission and reflection coefficients, along with a tunneling current vs distance graph from SNIPE. A square tunneling barrier is a good approximation of a real tunneling junction, so long as the work function of the tip and sample are similar [6].

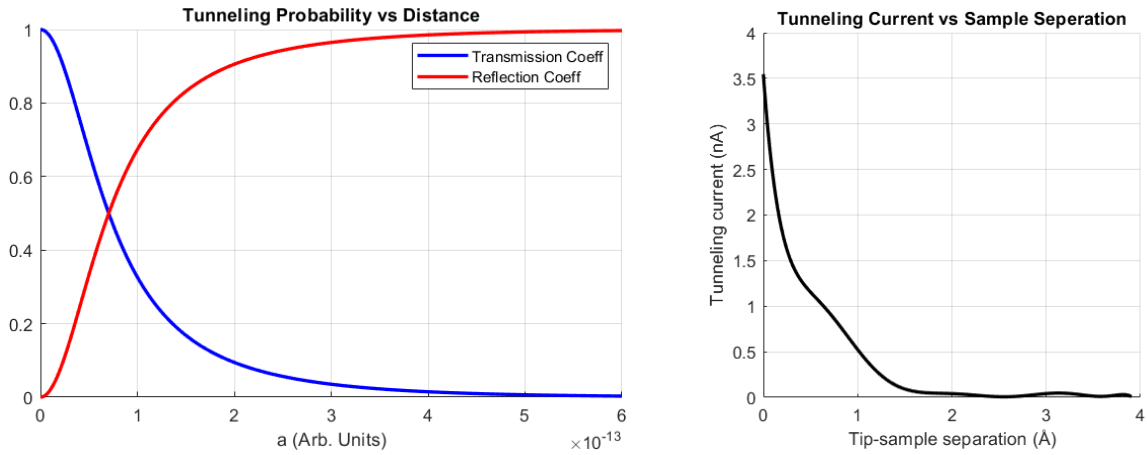

(a) (b)

Figure 1.3: (a) Plot of equations 1.12 and 1.13. Transmission coefficient is analogous to the tunneling probability. (b) Shows a real tunneling current vs tip-sample separation as taken from SNIPE. Note, the a=0 point is approximated to when current $i > 3.5nA$. $V_{bias} = 100mV$, $I_{inital} = 10pA$, tunneling junction is composed of a tungsten tip and an HOPG sample, both with work function $\phi \sim 5eV$.

The strong dependence of the transmission coefficient with tip-sample separation change is fundamental to STM's atomic imaging capabilities. If the transmission coefficient were roughly linear with a, creating a feedback loop to maintain constant current would be significantly more difficult given that the electrical noise would scale similarly to the tunneling current.

1.2 Overview of SNIPE

The scanning nanoscale interface probe ensemble (SNIPE) is a custom built scanning probe microscope (SPM) designed to work in high vacuum over a temperature range from 300K to 5K. At the heart of SNIPE is the Tyto SPM head made by Specs Group. Figure 1.4 shows an illustration of the system, which includes the SPM chamber assembly, and a sample preparation chamber which houses an heater and sputter gun.

The system was built in 2015 under the supervision of Professor Eric Hudson and operated until 2019 when an epoxy bond on the cryogenic dewar's cold finger failed. I started the restoration of SNIPE in January 2023. Now, in April 2024, the hardware on SNIPE is fully operational.

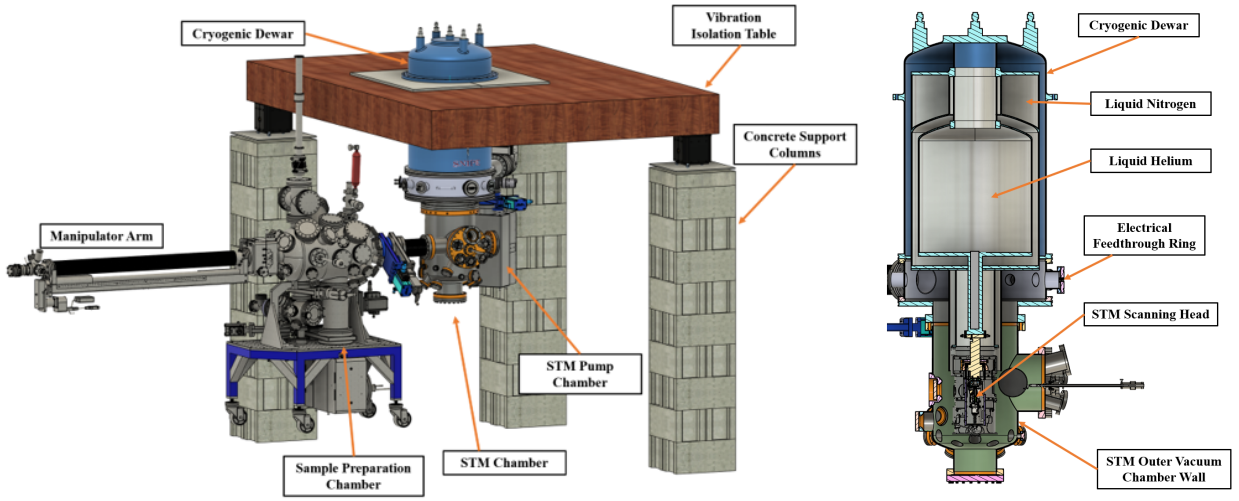

Figure 1.4: (a) Illustration of SNIPE. For scale, concrete columns are approximately 2m tall.(b) Cross section of SPM assembly.

1.2.1 SNIPE Restoration

In order to repair the dewar, it needed to be removed for welding. This involved a complete disassembly of the SPM chamber assembly. Once the Tyto head was removed, the dewar was lowered down from the vibration isolation table with a crane hoist, and shipped out for repair. Once the dewar returned in May 2023, the head was promptly reinstalled. The system was left vented while maintenance was performed on the delicate low microphonic coaxial wires that were damaged during the removal and reinstallation of the head. This time was also used to ensure the tube scanner and coarse motion on the Tyto was performing normally.

Once everything on the head was functioning, the chamber was put under vacuum. The first goal of the instrument in the testing stage was to achieve atomic resolution on highly oriented pyrolytic graphite (HOPG), a standard test surface for STM calibration. After a long process of troubleshooting the electronics, vibrations, and mechanics on the Tyto, the system finally achieved atomic resolution. During this process, Luc Schrauf, an incoming undergraduate, joined the lab and started helping me with the restoration process.

The sample preparation chamber's heater stage needed to be replaced due to a burnt heater

coil. Once the heater was replaced, the sputter gun was also set up and tested; Fig. 1.5 shows these repairs.

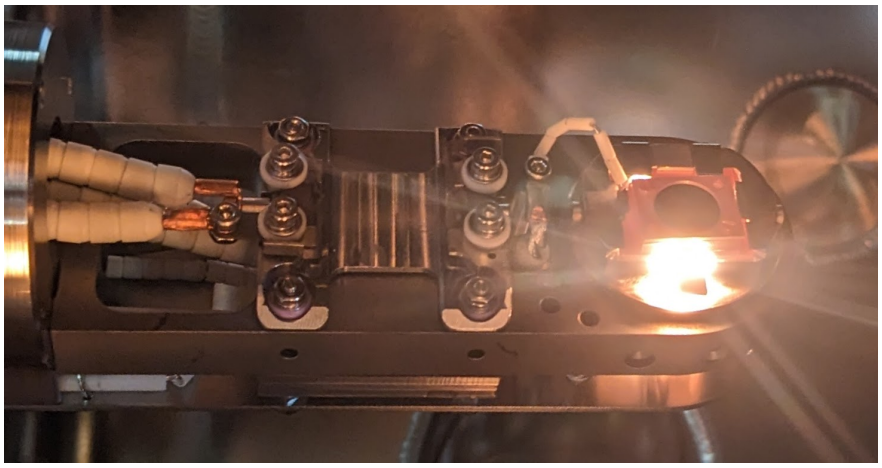

(a)

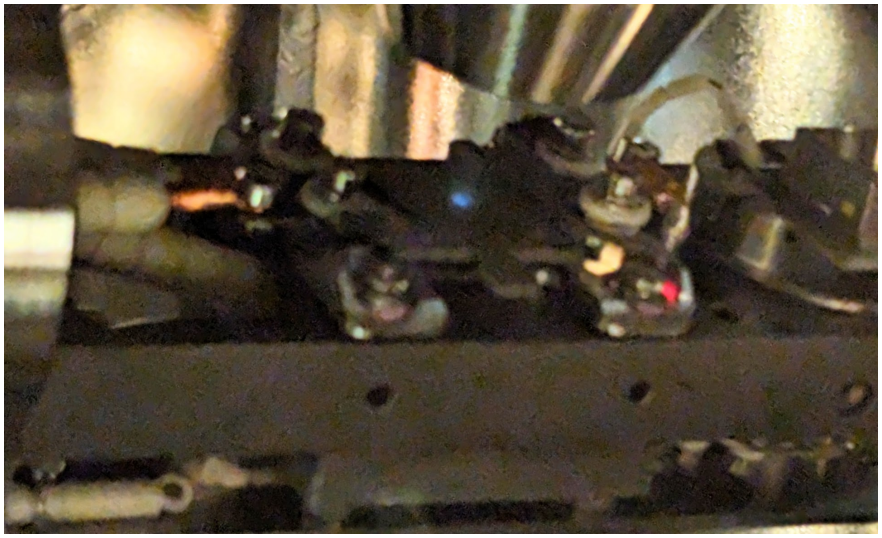

(b)

Figure 1.5: (a) Heater stage annealing a gold sample. (b) Argon sputter gun striking tantalum oxide which creates a blue luminescence. This is used to calibrate the magnetic lenses.

Unfortunately, a stainless steel to aluminum weld failed again on the dewar, and the entire repair process (including shipment of the deward back to the company for repairs) needed to be repeated. At the current stage, all the hardware on the system is functioning properly. In celebration of the restoration, the shipping crate built for the dewar was rapidly oxidized. Figure 1.6 shows an atomic resolution image on HOPG from testing, along with a photo of the radiation shield.

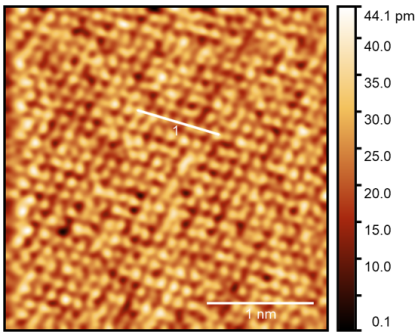

(a)

(b)

(c)

Figure 1.6: (a) Atomic resolution on HOPG from testing. Note, tube scanner was not calibrated in that image. (b) 77K radiation shield on SNIPE. (c) Celebratory rapid oxidation of dewar shipping crate.

With topographical imaging working, spectroscopic measurements were set up using an internal lock-in amplifier on the Nanonis control electronics. Figure 1.7 demonstrates working lock-in measurements primarily by a clean reconstruction of the I vs V curve. This sample was transferred from a growth chamber in air, and was exposed to air for approximately 20 minutes during the transfer. Ideally, the sample would be transferred under vacuum, which is possible to perform with the preparation chamber on SNIPE. Another way to achieve clean surfaces is by cleaving the sample in-situ by epoxying an aluminum post to the sample's surface, then striking the post with a wobble stick. Figure 1.8 shows a bulk bismuth selenide (Bi_2Se_3) sample that was cleaved in SNIPE's preparation chamber. Materials with weak interlayer bonding (known as van der Waals materials) can also be prepared in a similar fashion. HOPG is one such material, and this was prepared by adhering a strip of Kapton tape to the sample's surface in air. Then, the wobble stick is used to remove the strip of Kapton tape in-situ, thereby exposing an atomically clean surface on the sample. This method is known as exfoliation.

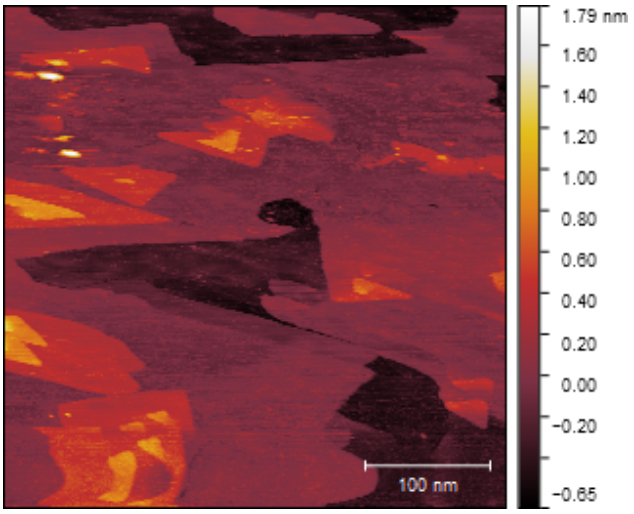

(a)

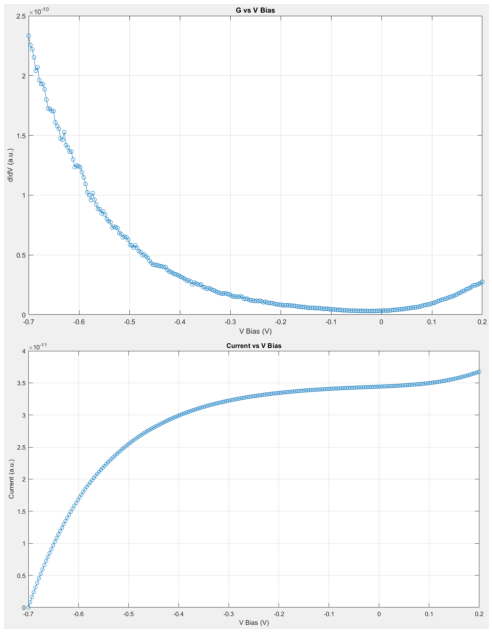

(b)

Figure 1.7: (a) Topography of molecular beam epitaxy (MBE)-grown Bi_2Se_3. Doubling of features is an artifact of the tip. (b) Spectroscopic point measurement using lock-in amplifier (top). Reconstructed current vs bias curve from the dI/dV lock-in measurement (bottom).

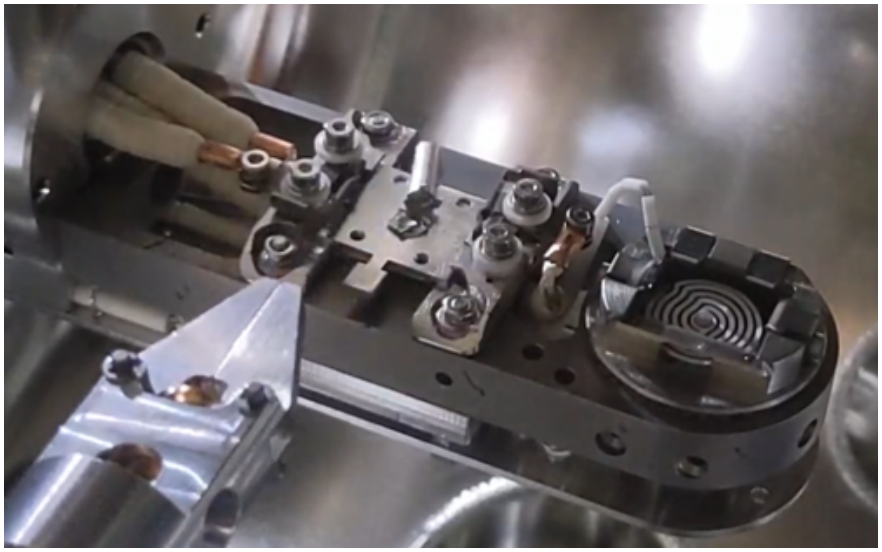

Figure 1.8: Bulk Bi_2Se_3 after being cleaved using SNIPE's wobble stick to strike the aluminum post off the sample, exposing an atomically clean surface.

Chapter 2

Automated Tungsten Tip Etcher

2.1 Introduction

The performance of an STM relies critically on atomically sharp tips so that the tunneling current is spatially confined to tunneling into atoms directly below the tip. Not only does the tip need to be atomically sharp, it is also important that the tip be conductive. Stability is especially important for performing spectroscopic measurements such as bias sweeps and distance sweeps when large changes in current are common. Tunneling measurement stability is largely determined by the absence of insulating contaminants (viz. oxides and water), while the spacial resolution is determined by the tip geometry. Here, I develop procedures to fabricate sharp tips, along with *ex-situ* processing which removes the tungsten trioxide layer deposited during fabrication.

2.2 Tip Etching

Chemical etching of tungsten is performed in 2 molar sodium hydroxide (NaOH), where an electrode is placed in the NaOH at ground potential, and tungsten wire at a small DC bias is submerged into the NaOH. This starts an electrolytic reaction that etches away the tungsten wire. The chemical reactions at the cathode (submerged in NaOH), and the anode (tungsten wire) and the overall reaction are shown in equations 2.1 2.2 and 2.3. *Source for reactions: [7].*

$$\text{Cathode (Ground): } 6H_2O + 6e^- \rightarrow 4H_2^{(gas)} + 6OH^- \tag{2.1}$$

$$\text{Anode (Bias Potential): } W + 8OH^- \rightarrow WO_4^{2-} + 4H_2O + 6e^- \tag{2.2}$$

$$\text{Overall Reaction: } W + 2OH^- + 2H_2O \rightarrow 3H_2^{(gas)} + WO_4^{2-} \tag{2.3}$$

The reaction at the anode produces tungsten oxide (WO_4^{2-}), which is a hard, non-porous oxide that coats the tungsten wire during the etch. As the etch continues, tungsten oxide precipitates from etching close to the surface, and adheres to tungsten further below the surface, slowing etching in those regions. Thus the wire etches faster close to the surface, forming an impingement throughout the etch. Once the impingement is narrow enough, it is not able to support the weight of the wire below the surface. Because of this the wire breaks, forming the tip. Figure 2.1 shows an illustration of this process. When the wire separates from the impingement, etching must be terminated as quickly as possible in order to avoid blunting the freshly formed tip. Additionally, the weight of the wire below the impingement directly determines how narrow the impingement is at the time of separation, it is very important to keep the amount of wire below the surface consistent from etch to etch.

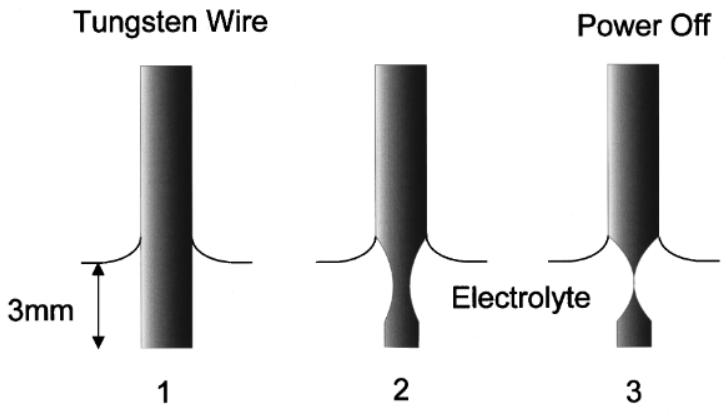

Figure 2.1: Tungsten wire submerged in etchant. Showing preferential etching and breaking of the wire to form the tip. Source [2].

2.3 Zyrus Etcher

I designed Zyrus to be an easy-to-use, reliable machine to fabricate etched tungsten tips. Zyrus uses an analog etching termination circuit, which uses two MOSFETs to start, and clamp the etching voltage at the moment the wire impingement breaks. With a constant etching voltage, the current slowly drops throughout the etch due to a reduction in surface area on the cathode. When the impingement breaks, there is a large change in current, which is detected by an operational amplifier (op amp) configured as a comparator. While the change in current (di/dt) is the most detectable feature, the cutoff circuit is acting on $i(t)$ since op amp differentiation circuits are susceptible to noise, and often require strong low pass filters. This adds circuit capacitance, which reduces the circuit's speed. A simplified schematic view of the analog cutoff circuit used on the etcher is shown in Fig. 2.2.

Figure 2.3 shows the speed of the cutoff circuit. The theoretical limit on the time response of the cutoff circuit is largely a function of the anode-cathode junction capacitance. When the p-channel MOSFET conducts after the comparator in Fig. 2.2a triggers low, the anode is shorted to ground with a low on resistance through the IRFD9120 (0.60Ω from [8]). However, the largest delay is in the comparator. An LF412CN operational amplifier was used as a comparator, and has a maximum slew rate (SR) of $15V/\mu s$ [9]. Since the IRFD9120 only conducts when $V_{GS} > 4V$,

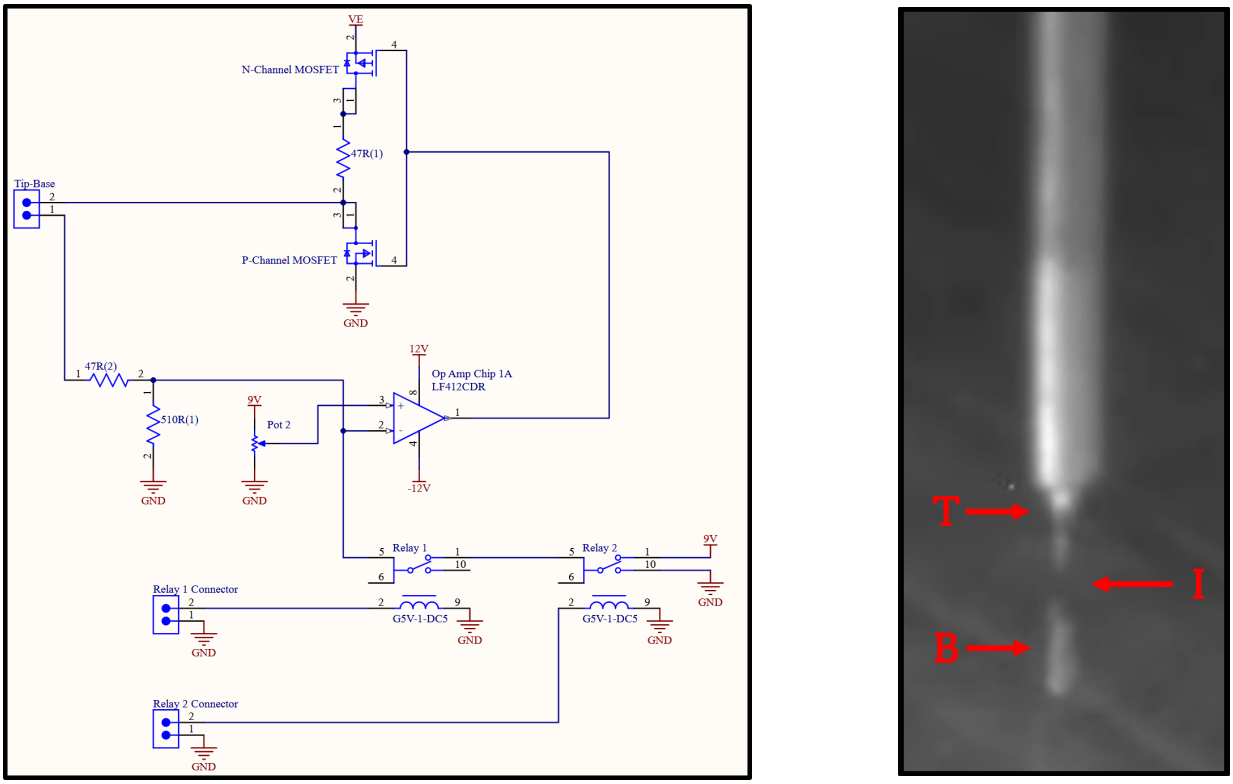

(a) (b)

Figure 2.2: (a) Simplified etching detection and termination circuit on Zyrus. (b) Wire being etched, 10 ms before breaking. Bottom of the wire labeled **B**, impingement region **I**, formed tip **T**. (Note: Etchant meniscus broken to make imaging easier in (b).)

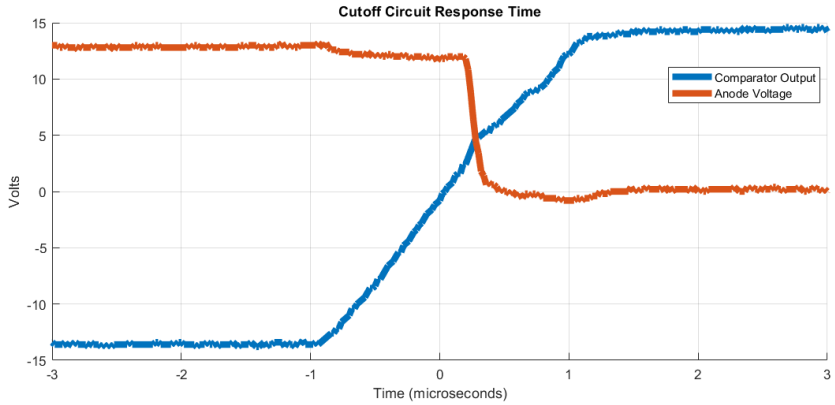

Figure 2.3: Response time of cutoff circuit. Blue plot is output of comparator, red curve is voltage on the tip. The time delay between the capacitor output rising and the anode voltage dropping to 0V defines the cutoff time, $1.5\mu s$.

the minimum switching speed is

$$\frac{V_{EE} + V_{GS}}{SR} = \frac{14V + 4V}{15V/\mu s} = 1.2\mu s. \tag{2.4}$$

Using a high speed op amp such as the OPA828 ($SR = 150V/\mu s$ [10]) could greatly reduce the cutoff time. Since the cutoff time of the rest of the circuit is $0.3\mu s$, the junction capacitance at the time the impingement breaks is approximately

$$3RC = \Delta t \rightarrow C = \frac{\Delta t}{3R} = \frac{0.3\mu s}{3 * 0.8\Omega} = 0.2\mu F. \tag{2.5}$$

The next criterion for making repeatable tips is controlling the wire submerging distance. This is done by having a motorized stage to submerge the wire in a controlled manner. As an etch is started, the machine measures the voltage between the tungsten wire and etchant. When the anode is not in contact with the cathode, the anode is held at ground potential through a pull down resistor. Then, the wire is lowered toward the liquid, and a microcontroller monitors the voltage on the anode. Once the wire makes contact with the etchant, the wire voltage rises above 0 V. Then, the motorized z-stage drives the wire below the surface to a predefined amount (1-4mm). With this, the submersion depth can be repeatably controlled within $50\mu m$.

The last criterion for making consistent, symmetrical tips is a symmetric electric field in the etchant dish. Zyrus accomplishes this by using a 2" diameter cathode made of stainless steel. Small variations in the cathode shape will cause non-uniform electric fields close to the cathode, but since the anode is far away at the center of the circular cathode, the electric field will be more uniform. Figure 2.4 shows an image of Zyrus during an etch.

2.4 Tip Preparation for STM

After etching, the tips have electrically insulating tungsten oxide layers on them (see equation 2.2) which would be problematic for performing STM. There are multiple ways to remove the

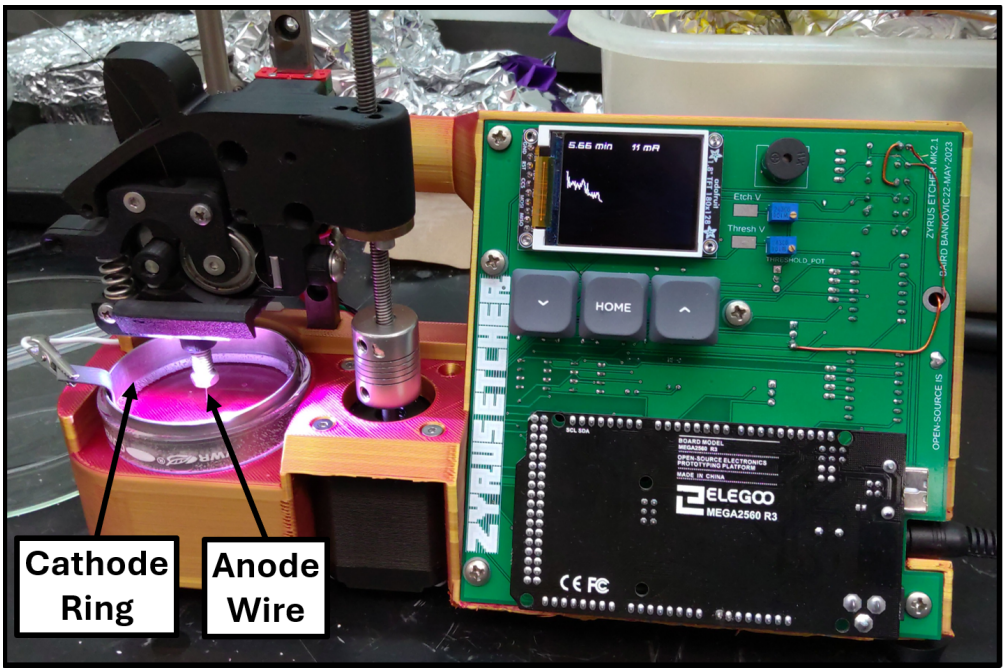

Figure 2.4: Zyrus Etcher performing an etch.

oxide layer *in-situ* such as field emission, annealing, or sputtering. After loading a freshly etched tip without any attempt to remove the oxide layers, the tunneling current is unstable and the PID feedback control is not sufficient to maintain constant current for topographic imaging. However, I found that submerging the tips in a strong acid such as hydrochloric acid (HCl), then rinsing them in deionized water removed enough of the oxide such that tips would be stable immediately upon landing in the STM. From there, light voltage pulsing ($\pm 10V$ to $\pm 2V$) would be sufficient to bring the tip into atomic resolution. Figure 2.5 shows scanning electron microscope images of two tips with different post-etch treatments. An example of this procedure being followed on highly ordered pyrolytic graphite (HOPG) is shown in Fig. 2.6. More details on procedures and open-source files can be found at [11] and [12].

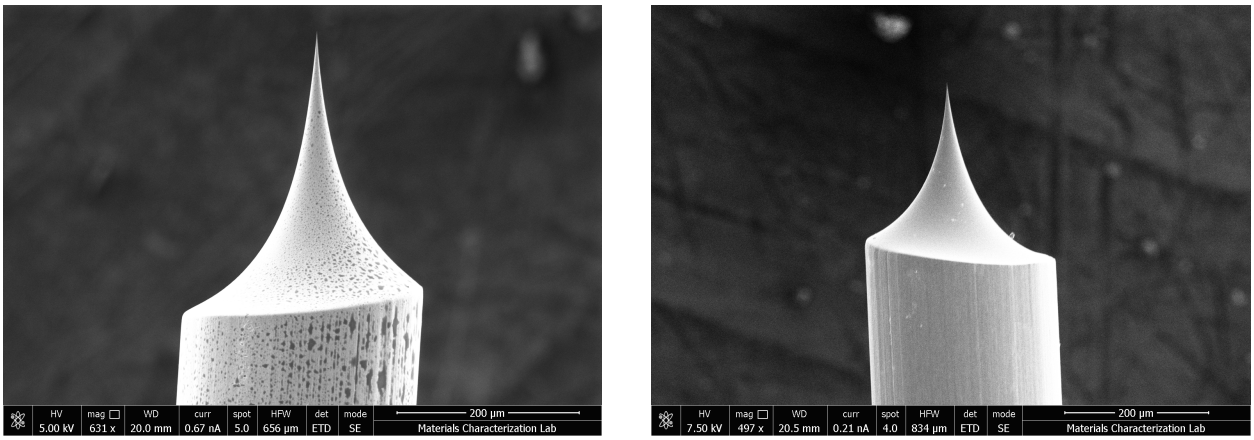

(a) (b)

Figure 2.5: Tips etched on Zyrus. (a) Imaged after etching with just a deionized water rinse. (b) Tip submerged in HCl for approximately 30 seconds after etching, then rinsed with deionized water. Black spots on tip (a) are regions of oxides and organics, where tip (b) appears much cleaner.

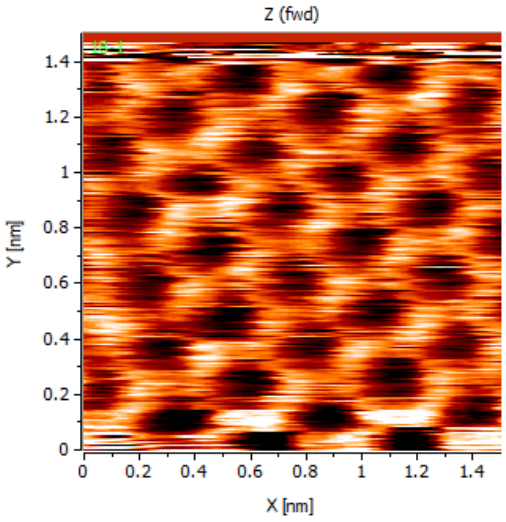

Figure 2.6: Atomic resolution on HOPG with a tip from Zyrus.

Chapter 3

In-situ Transimpedance Preamplifier

3.1 Motivation

An STM requires precise, low noise measurements of small currents ($1pA - 1nA$). In order to reduce pickup noise along long analog lines which run from the STM head to outside the vacuum space, positioning the tunneling current amplifier inside the vacuum and as close to the head can lower the noise floor. However, many measurements either benefit or require low temperatures, and an amplifier that is vacuum compatible, works at low temperatures, and has sufficiently high bandwidth makes for a uniquely difficult set of constraints. This chapter outlines the construction of a transimpedance amplifier which can be mounted on the head of the STM and has stable performance from room temperature (300K) to liquid nitrogen temperature (77K).

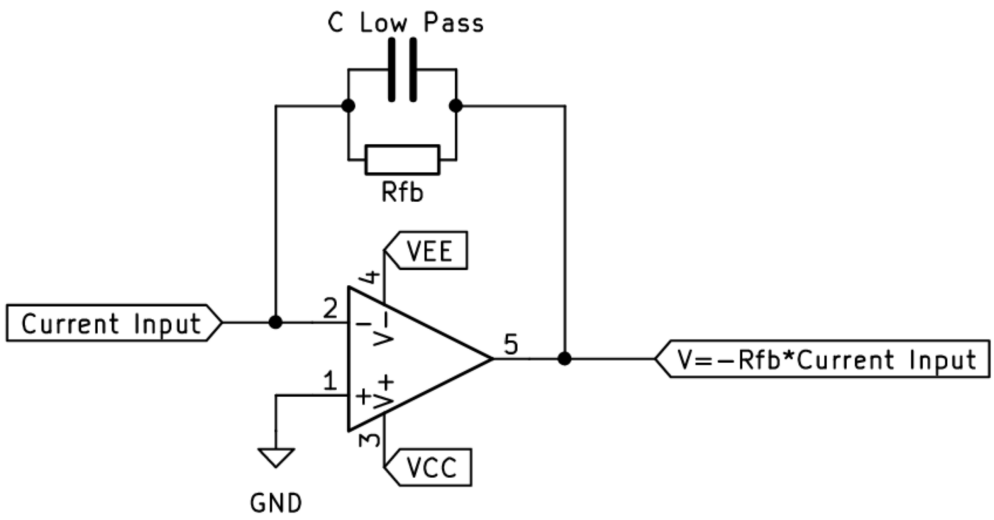

Figure 3.1: Schematic of transimpedance amplifier with common ground. $V_{out} = -I_{in}R_{fb}$

3.2 Operational Amplifier Roundup

Figure 3.1 shows a schematic of a simple linear transimpedance amplifier (TIA) using an operational amplifier (op amp) in negative feedback. Often times, TIAs in this configuration exhibit large instabilities. To reduce device instabilities, a small value capacitor is placed across the feedback resistor to act as a first order low pass filter.

When selecting an op amp for the TIA, it is important for the op amp to have low input bias current (<1pA), high open-loop gain ($> 10^5$), and sufficient bandwidth for dI/dV measurements (>1kHz). While these parameters can be found on the manufacturer's datasheet, performance below -40 C is not guaranteed. The operational amplifier roundup project selected the top performing op amps for TIAs, and tested them at low temperature in order to see which op amps are suitable for low temperature use.

3.2.1 First Round - LN2 Submersion

All the op amps were first tested by submerging them in liquid nitrogen (LN2), and measuring the TIA response in the form of a Bode plot. Figure 3.2a shows the testing rig for submerging op amps in a dual in-line package (DIP). Each op amp was tested at room temperature, and then

Device	Behavior in LN2 Submersion
LMC6035	Insulating
MAX4424	Insulating
MAX9945	Large output bias
AD8627	Large output bias
AD8626	Large output bias
AD8641	Oscillations $< 1kHz$
ISL2811	Oscillations $< 1kHz$
OPA140	Performed nominally
OPA2140	Performed nominally
LT1464	Insulating
TLE2072	Mild output bias
OPA828	Mild output bias
OPA2828	Mild output bias
CA3420	Insufficient Gain-bandwidth product

Table 3.1: Round one, mA testing of devices configured as TIAs with $R_{fb} = 10k\Omega$.

immediately afterward at 77 K. Then, features on the Bode plots and the time domain waveform were compared for obvious deviation from normal operation. Since the feedback resistor was being submerged, changes in gain and the bandwidth cannot be interpreted as a change in the op amp's performance, but clear unstable operation indicates a failure in the device physics (viz. carrier freeze-out, slow switching speed). Table 1 shows a summary of the first round of device testing.

3.2.2 Second Round - Low Current

Devices that performed similarly at room temperature and at 77 K were selected for the next round of testing. This round focused on device performance at low currents (1 nA), and places the feedback resistor out of the LN2 bath. A small DIP stick was made so that the distance from the op amp to the feedback resistor was short enough not to induce instability and noise in the measurements. Figure 3.2b shows the testing configuration for these op amps. Since the feedback resistor is kept out of the LN2 bath, changes in close-loop gain and bandwidth are a result of anomalous behavior of the op amp. The devices under test were the OPA140, OPA2140, OPA828, TLE2072, and the MAX9945. The OPA140 and OPA2140 are very similar, being the single and dual op amp version in the same foot print. Both op amps exhibited stable performance in LN2

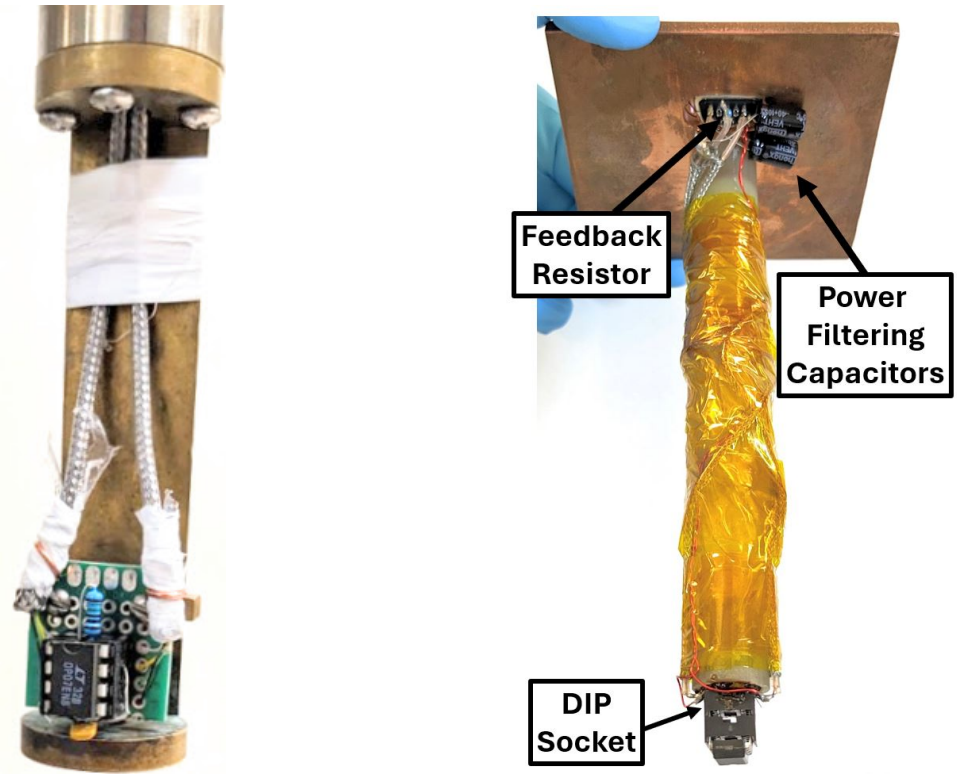

(a) (b)

Figure 3.2: (a) DIP stick for mA currents. (b) Configuration for nA TIA testing with feedback resistor kept close to room temperature.

submersion. Finally, the MAX9945 develops a significant voltage offset at 77K ($\sim$ 5mV), but due to its high speed (45 MHz), it is still of particular interest despite the large offset.

Overall, device performance did not differ much from testing done at higher currents.

3.2.3 Final TIA Design

Since the OPA828, OPA140, TLE2072, and the MAX9945 all survived LN2 submersion, they are all candidates to be used as a low temperature STM preamplifier. The first TIA to be tested was the OPA140 since it had very little offset voltage at low temperature. Figure 3.3a shows the TIA.

A 3 pF capacitor was placed in parallel with the feedback resistor to increase stability at high frequencies. At low frequencies, the capacitor has a high impedance, and current is passed through the feedback resistor. However, a sufficiently high frequency current on the feedback net will see a low impedance on capacitor, and is amplified with close to unity gain. Therefore, adding a

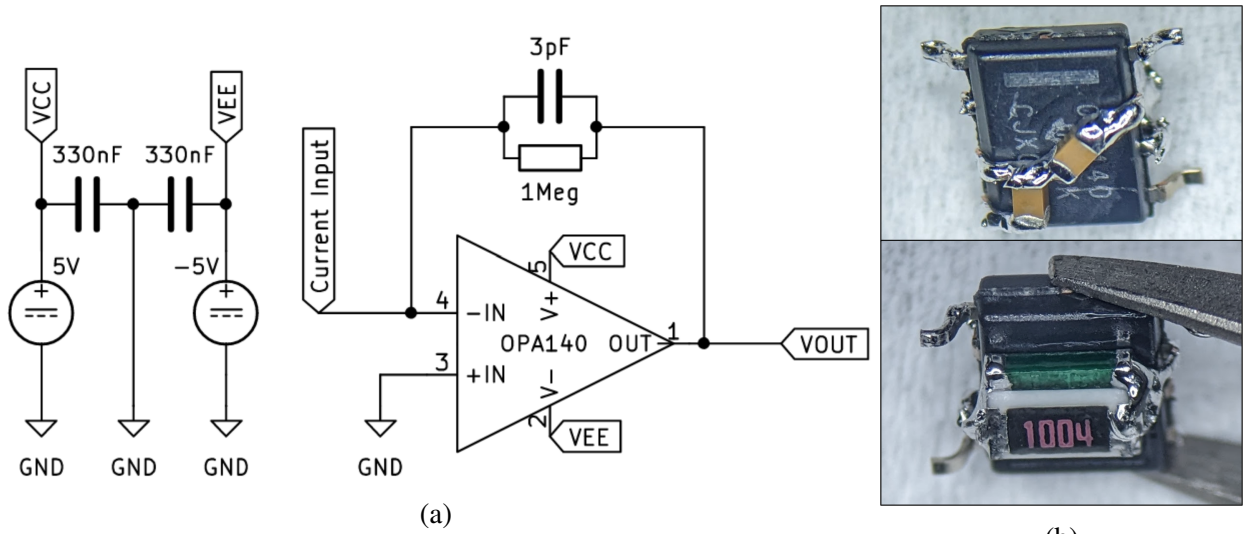

(a) (b)

Figure 3.3: (a) Shows schematic view of TIA. (b) Shows physical implementation of (a) in a compact form to do testing in cryostat.

capacitor in the feedback loop acts as a low pass filter. This TIA was tested in a DynaCool physical properties measurement system (PPMS) at successively lower temperatures until failure. Figure 3.4 shows the gain response of the OPA140 based TIA. The noise floor of the TIA could not be measured due to microphonic electrical noise on the DynaCool due to its pulse tube cryocooler design.

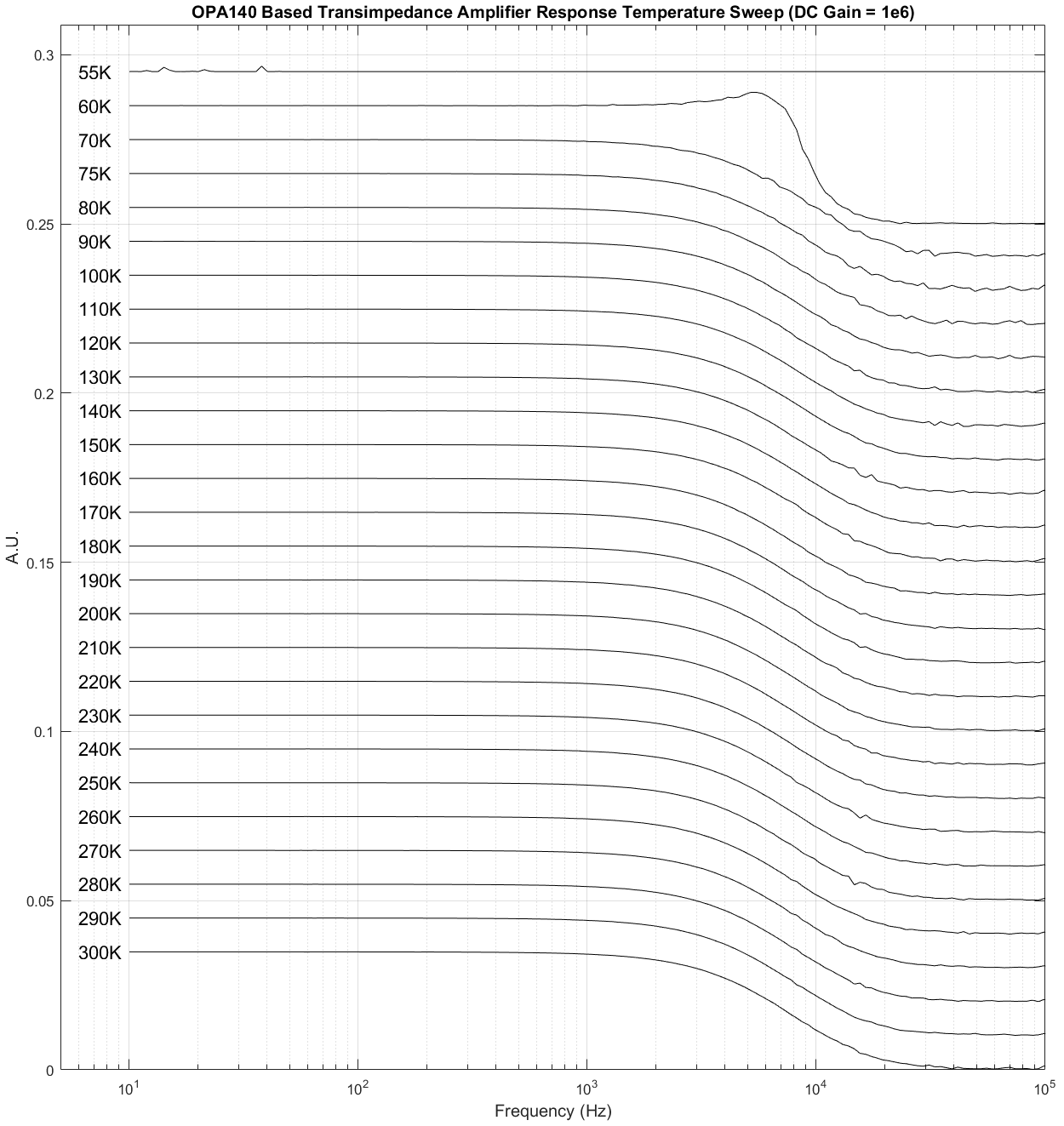

Figure 3.4: Temperature response of OPA140 based TIA. Device failed just above 55K, where the Bode plot shows insulating behavior. (Note: 55K plot shifted for readability.)

Chapter 4

Conclusion

Now that SNIPE is in use once again, it can be used to study quantum materials. While the STM is operational, there are still plans for hardware upgrades. Next month, (April 2024), the transimpedance preamplifier should be ready for installation in the vacuum chamber next to the Tyto. This will also coincide with first cool down SNIPE has seen since 2019. The low temperature preamplifier should increase the signal to noise ratio (SNR), along with reducing 60Hz noise which is present due to poor grounding in the lab.

The Tyto SPM head has a unique capability because of its modular scanning probe sensors. The Tyto has a commercial sensor package called the Kolibri sensor, which is a high performance 1 MHz, ultra low amplitude ($\sim 2pm$) atomic force microscope (AFM) sensor that is compatible with the Tyto. However, this sensor package has a considerable operating cost due to its non-replaceable tips. Luc Schrauf, the next student and operator of SNIPE, will be building a custom low-cost AFM sensor for the Tyto based on commercial quartz tuning fork oscillators, similar to the first qPlus AFM sensors created by Franz Giessibl in 1998 [13]. This will make SNIPE the only low temperature AFM system at Penn State, along with the capability to perform STM and AFM

at the same time. This is useful since AFM tracks the real topography of a sample, whereas STM is sensitive to only the electronic structure. Using AFM to maintain constant distance from the sample can add additional stability to measurements on rough surfaces, along with higher speed topography image acquisition. I anticipate that this extension of SNIPE will be a satisfactory conclusion to the work I carried out in restoring SNIPE to near normal working condition.

Bibliography

[1] How does an atom look under the scanning tunnel microscope? https://www.quora.com/What-is-a-scanning-tunneling-microscope. Accessed: 26 Feb 2023.

[2] Rei Hobara, Shinya Yoshimoto, Shuji Hasegawa, and Katsuyoshi Sakamoto. Dynamic electrochemical-etching technique for tungsten tips suitable for multi-tip scanning tunneling microscopes. *E-journal of Surface Science and Nanotechnology*, 5:94–98, 2007.

[3] Erwin W. Müller and Kanwar Bahadur. Field ionization of gases at a metal surface and the resolution of the field ion microscope. *Phys. Rev.*, 102:624–631, May 1956.

[4] G. Binnig, H. Rohrer, Ch. Gerber, and E. Weibel. Tunneling through a controllable vacuum gap. *Applied Physics Letters*, 40(2):178–180, 1982.

[5] How to move an atom. https://www.ibm.com/blogs/research/2013/05/how-to-move-an-atom/. Accessed: 2023-02-08.

[6] Joseph A. Stroscio and William J. Kaiser. *Scanning Tunneling Microscopy*. Academic Press Limited, 24-28 Oval Road, London NW1 7DX, 1993.

[7] Stm tip preperation. https://www.bc.edu/content/bc-web/schools/morrissey/departments/physics/labs/Zeljkovic-Lab/research/stm-tip-preparation.html. Accessed: 1 April 2024.

[8] Visha Siliconix. *Power MOSFET*, 8 2021. S21-0887-Rev. F.

[9] Texas Instruments. *LF412-N Low Offset, Low Drift Dual JFET Input Operational Amplifier*, 7 2014. SNOSBH7F.

[10] Texas Instruments. *OPAx828 Low-Offset, Low-Drift, Low-Noise, 45-MHz, 36-V, JFET-Input Operational Amplifiers*, 12 2022. SBOS671D.

[11] Robin Kearey. Homebrew probe tip etcher makes amazingly sharp needles. https://hackaday.com/2023/09/14/homebrew-probe-tip-etcher-makes-amazingly-sharp-needles/. Accessed 1 April 2024.

[12] Baird Bankovic. Zyrus etcher, stm tip fabricator. https://www.youtube.com/watch?v=2C8MTMYGBhw. Accessed: 1 April 2024.

[13] Franz J. Giessibl. High-speed force sensor for force microscopy and profilometry utilizing a quartz tuning fork. *Applied Physics Letters*, 73(26):3956–3958, 12 1998.